

Thermo-responsive Black VO₂-Carbon Nanotubes Composite Coatings for Solar Energy Harvesting

Vasu Prasad Prasadam, Francisco V. Ramirez,^a Ioannis Papakonstantinou,^a Ivan P. Parkin,^a Naoufal Bahlawane

Material Research and Technology Department, Luxembourg Institute of Science and Technology,
Rue du Brill, L-4422 Belvaux, Luxembourg

^a Photonic Innovations Lab, Department of Electronic and Electrical Engineering, University College
London, Torrington Place, London, WC1E 7JE, UK

Abstract

Solar energy harvesting is an essential component for clean and sustainable future energy supply. Hereby, solar thermal energy conversion is of a significant importance, and the role of absorbing layers is pivotal. Nanoscale design of thermally responsive absorbing nanocomposite coatings is addressed in this study with the objective to tailor the light absorption behaviour. While carbon nanotubes (CNTs) act as perfect black absorbers, vanadium dioxide (VO₂) shows a semiconductor-to-metal transition (SMT) at 67 °C with an abrupt change in the optical properties. Combining the properties of these two nanometric building blocks is investigated as an approach to design smart black nanocomposite films. The CNTs feature either an upward or downward thermal emissivity switching across the SMT depending on the morphology of the overgrown VO₂ nanolayer. Decorated CNTs with VO₂ nanoparticles feature an enhancement of the thermal emissivity above the SMT, whereas VO₂-covered CNTs feature a decrease of thermal emissivity when they turn metallic above the SMT. The results were successfully explained by a theoretical model based on effective media approximations. By means of this model, the percolation threshold for the VO₂ inclusions was identified. VO₂ inclusions below this threshold are mostly confined in small domains and near/mid infrared light absorption dominates in the metallic phase, as a consequence of localized surface plasmons excitation. Above the percolation threshold, VO₂ inclusions form large continuous domains that are more reflective in the metallic phase. The percolation threshold is the result of surface-energy-driven dewetting that can be influenced by the implemented thermal treatment. The developed VO₂-CNTs nanocomposite films hold appealing properties for the design of smart absorbers for solar energy harvesting and thermal management, as well as photo-thermal actuators

Keywords: Solar absorbers, thermal radiation, smart absorber, smart radiators, nanocomposite coatings, CNT, SMT, Vanadium oxide, CVD, ALD.

Introduction

The continuous growth of the global electricity demand implies a consequent rise of energy production leading to a record CO₂ emission increase, +1.7 %/annum in 2018¹. Sun, which is the most abundant clean source for energy, can be harnessed through a direct conversion to electricity (Photovoltaics) or through thermal energy. The approach of adjusting or modulating solar energy gave rise to valuable applications such as, solar selective absorber in thermoelectric devices², solar thermal radiator for cooling devices³, and smart coatings for energy efficient windows⁴. Generally, these nanocomposite coatings incorporate materials with contrasting optical properties to engineer the targeted functionality.

The implementation of carbon nanotubes (CNTs) and vanadium dioxide (VO₂) as building blocks to design smart absorbing coatings sounds appealing in this context. CNTs feature a near perfect black body absorption⁵, nevertheless, their sole implementation is not sufficient to harvest solar energy, as CNTs are also great thermal emitters. On the other side, VO₂ features an abrupt change in its optoelectronic properties across its semiconductor-to-metal transition, which takes place at 67 °C^{6,7}. In fact, metals are typical good infrared (IR) reflectors and semiconductor are mostly NIR transparent.

A simulation study reported by Voti et al reveals that stacks involving VO₂ and metallic layers can be engineered to optimize an up- and down-ward thermal emissivity depending on the stack architecture⁸. The expected downward emissivity modulation, i.e. emissivity ($E_{\text{hot}} - E_{\text{cold}}$) < 0, is reported using VO₂ film with a thickness exceeding 100 nm on different IR transmitting substrates like Si⁹, quartz¹⁰, graphene¹¹, TiN¹² and Al₂O₃¹³. An upward emissivity modulation, i.e. emissivity ($E_{\text{hot}} - E_{\text{cold}}$) > 0, was however reported using IR reflecting substrates¹⁴. Incorporating an intermediate dielectric layer in the last case amplifies the emissivity modulation response^{15,16}. Surfaces featuring textures with high aspect ratios are particularly appealing as the amplitude of the optical modulation is expected to be more prominent^{17,18}. Based on the emissivity modulation down or upward, the resulting composites might be used in different applications like smart windows¹⁹ and smart radiators²⁰ for terrestrial and space application respectively.

Vanadium dioxide-Carbon composites have potential application in various fields as: electrode materials for energy storage^{21,7}, gas sensors²², infrared detectors²³, thermal camouflage¹¹ and photo-thermal actuators^{24,25,26,27}. In the above-mentioned literature, VO₂ is grown on carbon films by the chemical sol-gel, physical vapour deposition techniques. To grow conformal VO₂ layers on the high aspect ratio structures, atomic layer deposition (ALD) is the most reported process⁷.

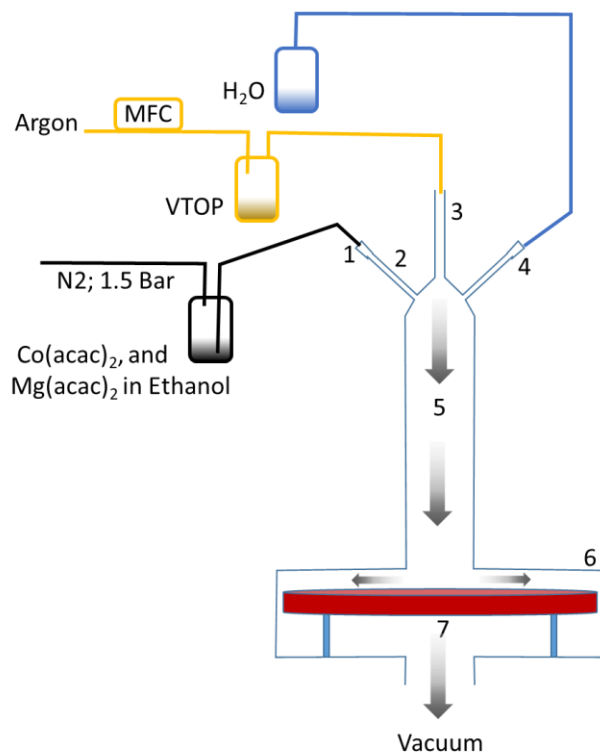
In the present study, a strongly correlated material (VO₂) is applied on highly textured black absorber coating, CNTs, to investigate the optical modulation behaviour based on fundamentally contrasting

classical and plasmonic optical response. The chemical vapour deposition (CVD) process is used for the growth of CNT layers, whereas, the atomic layer deposition process (ALD) was used to grow conformal VO₂ layers around the individual CNTs of the film.

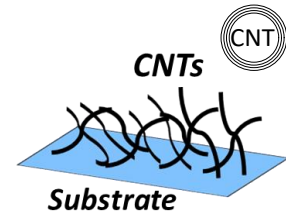
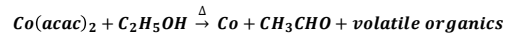
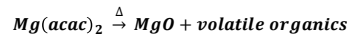
Experimental method

The deposition of carbon nanotubes on silicon substrates was performed using the thermal CVD process. Hereby an ethanol solution of $0.65 \times 10^{-3} \text{ mol L}^{-1}$ of cobalt acetylacetonate (Co(acac)₂) and $0.65 \times 10^{-3} \text{ mol L}^{-1}$ of magnesium acetylacetonate (Mg(acac)₂) was implemented as a single precursor feedstock. The formation of CNTs is obtained at 485 °C and a pressure of 10 mbar with ethanol vapour as the carbon source in the presence of a cobalt catalyst and MgO growth promoter, both form in situ during deposition. The CVD of CNT is illustrated in Scheme 1. The layer is composed of randomly oriented CNTs featuring an adjustable density²⁸. The implemented CNT films in this study have an average thickness of 3 μm and a density of 0.8-1 mg/cm³, whereas the outer diameter of the CNT is around 10 nm. It is worth mentioning that the obtained film density is three orders of magnitude lower relative to densely packed CNTs. Further details regarding the process are reported earlier²⁹.

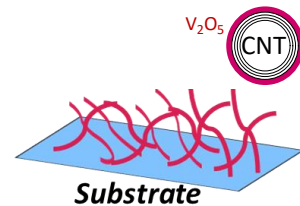
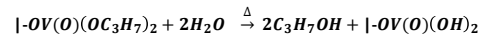
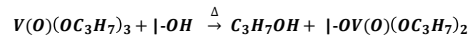
Vanadium oxide films are deposited on CNTs using thermal ALD via the sequential hydrolysis with de-ionized water, of Vanadyl (V) triisopropoxide (VTOP) at 80 °C and a pressure of 0.4 mbar. All depositions were performed using ALD cycles composed of: (a) 8 s exposure to VTOP, (b) 15 s of argon purge gas with a flow rate of 50 sccm, (c) 6 s exposure to water vapour and (d) 15 s argon purge. The as-grown films were identified as amorphous or poorly crystalline V₂O₅. Details of the ALD optimisation on planar Si substrates are reported earlier³⁰. The ALD consecutive reactions are displayed in Scheme 1.



Chemical Vapour Deposition (CVD)



Atomic Layer Deposition (ALD)



Scheme 1. Illustration of the hybrid CVD/ALD experimental setup for the growth of the CNT-based nanocomposite. The right-hand side presents the involved two steps, the corresponding chemical reactions and the materials structure. [1- Pulsed spray injector (opening time 4ms; frequency 4Hz; rate 1ml/min); 2- Evaporation tube (at 200°C); 3- VTOP gas vapour inlet; 4- H₂O gas vapour inlet; 5- Transport tube (at 200°C); 6- Vacuum deposition chamber; 7- Hot substrate holder]. The main structural

Post deposition annealing was performed in vacuum (10^{-2} mbar) at 500 °C for 4 h to convert the as-grown film to crystalline VO₂-CNTs. The thickness of VO_x on silicon was assessed using multi-wavelength Ellipsometer (Film Sense) with the Cauchy model, whereas X-ray diffraction (Bruker D8), with Cu-K_α as the X-ray source, was used to identify the crystalline phases of vanadium oxide. Data were collected in the grazing incidence mode at 0.5° and a detector scanning from 20° to 60° with a step size of 0.02°.

All XRD reflexes of VO₂, except the (011) plane at 27.83°, can be attributed to overlapping planes, which complicates the implementation of the Williamson-hall method to assess the strain and crystallite size values. Hence, the single peak analysis method was used. The broadening of the XRD peak is a combined contribution from the instrumental broadening, strain in the lattice and size of the crystallites. Thereby we defined 0.173 as the instrumental broadening measured using single crystal silicon wafer. We fit the VO₂ (011) peak to pseudo voigt1 function, which is a linear combination of Lorentzian and Gaussian functions. The peak deconvolution provides the broadening resulting from the size effect (Lorentz component with β_L) and that resulting from the strain effect (Gauss component

with β_G). Both are the corrected FWHM of both components from the instrumental broadening as follow: $FWHM_L = \beta_L + \beta_I$; and $(FWHM_G)^2 = (\beta_G)^2 + (\beta_I)^2$.

The crystallite size, d , and the strain, ε , are computed using the following equations:

$$d = \frac{K\lambda}{\beta_L \cos \theta}; \varepsilon = \frac{\beta_G}{4 \tan \theta} \quad \text{Eq. (1)}$$

We assume $\kappa = 0.94$ and $\lambda = 0.154$ nm (Cu α).

Raman scattering was performed using an InVia Raman spectrometer from Renishaw with a 633 nm laser and a power density of 87 $\mu\text{W}/\text{cm}^2$. The morphology of the films was inspected using the FEI Helios Nanolab 650 scanning electron microscope (SEM) at a working distance of 5 mm and using 2-5 V as the acceleration voltage.

The surface emissivity was measured using FLIR X6580SC thermal camera operating in the 3-5 μm spectral range. The pristine CNTs coating was taken as a reference perfect black in these measurements. The emissivity measurement was performed along three consecutive heating and cooling cycles between 30 $^\circ\text{C}$ and 85 $^\circ\text{C}$ using a ramping rate of 2 $^\circ\text{C}/\text{min}$. The optical measurements were carried out in a reflection configuration using LAMBDA 1050 UV-VIS-NIR spectrophotometer from Perkin Elmer with a 100 mm Spectralon integration sphere. Measurements were performed in the 300–2300 nm spectral range, while the surface temperature was cycled between 25 $^\circ\text{C}$ and 95 $^\circ\text{C}$.

Theory Methods

The effective permittivity of the CVD-grown CNT film is estimated by³¹:

$$\varepsilon_{\perp}^{eff} = \varepsilon_h \left(1 + f_{\text{CNT}} \frac{\alpha}{1 - f_{\text{CNT}} L \alpha} \right) \quad \text{Eq. (2a)}$$

$$\varepsilon_{\parallel}^{eff} = f_{\text{CNT}} \varepsilon_o + (1 - f_{\text{CNT}}) \varepsilon_h, \quad \text{Eq. (2b)}$$

where ε_h is the host material surrounding the CNT, f_{CNT} is the filling fraction of the CNT, $L = 1/2$ is the depolarization factor, and α is the 2D polarizability of the CNT³²:

$$\alpha = \frac{2}{1 - \rho^2} \cdot \frac{(\varepsilon_e \Delta - 1)(\varepsilon_e \Delta + \varepsilon_h) \rho^{2\Delta} - (\varepsilon_e \Delta - \varepsilon_h)(\varepsilon_e \Delta + 1)}{(\varepsilon_e \Delta - 1)(\varepsilon_e \Delta - \varepsilon_h) \rho^{2\Delta} - (\varepsilon_e \Delta + \varepsilon_h)(\varepsilon_e \Delta + 1)} \quad \text{Eq. (3)}$$

here, $\rho = r/R_{\text{CNT}}$, is the ratio between the inner, r , and outer, R_{CNT} , CNT radius. The parameters ε_o and ε_e are the dielectric constant of graphite at the ordinary (perpendicular) and extraordinary (parallel) axis, respectively, and $\Delta = \sqrt{\varepsilon_o/\varepsilon_e}$. The filling fraction is determined by³³: $f_{\text{CNT}} = \pi \left(\frac{R_{\text{CNT}}}{a} \right)^2 (1 - \rho^2)$, where a is the lattice constant of the 2D array.

Eq. (2) is based on a 2D array of CNTs, and therefore it represents an anisotropic media. For low CNTs filling fractions, the effective permittivity of randomly aligned structures can be approximated by³⁴:

$$\varepsilon_{\text{eff}} = \frac{1}{3}\varepsilon_{\perp}^{\text{eff}} + \frac{2}{3}\varepsilon_{\parallel}^{\text{eff}} \quad \text{Eq. (4)}$$

The change in the optical properties induced by the VO₂ inclusions is included by the dielectric constant of the host material, ε_h , by using Bruggeman's effective media theory for a VO₂–air composite³⁵:

$$f^* \frac{\varepsilon_{\text{VO}_2} - \varepsilon_h}{\varepsilon_{\text{VO}_2} + 2\varepsilon_h} + (1 - f^*) \frac{\varepsilon_{\text{air}} - \varepsilon_h}{\varepsilon_{\text{air}} + 2\varepsilon_h} = 0, \quad \text{Eq. (5)}$$

where $\varepsilon_{\text{air}} = 1$ is the dielectric constant of air, $\varepsilon_{\text{VO}_2}$ is the dielectric constant of VO₂, and $f^* = \frac{1}{1 - \pi(R_{\text{CNT}}/a)^2} f_{\text{VO}_2}$, corresponds to a fraction of VO₂ relative to the volume outside the CNT's. The filling fraction of VO₂ relative to the unit cell, f_{VO_2} is given by:

$$f_{\text{VO}_2} = \frac{\pi \left[(R_{\text{CNT}} + t_{\text{VO}_2})^2 - R_{\text{CNT}}^2 \right]}{a^2},$$

where t_{VO_2} is the thickness of the ALD-deposited VO₂ layer (assuming the coating is uniformly distributed over the CNT surface), which is estimated by the product of the ALD deposition rate and number of cycles. Here and in the rest of the paper, the term “filling fraction” corresponds to f_{VO_2} .

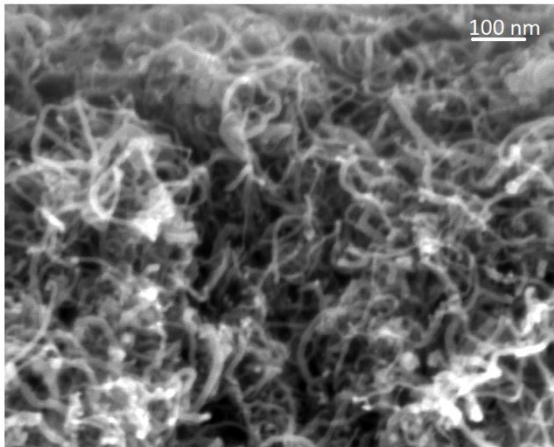
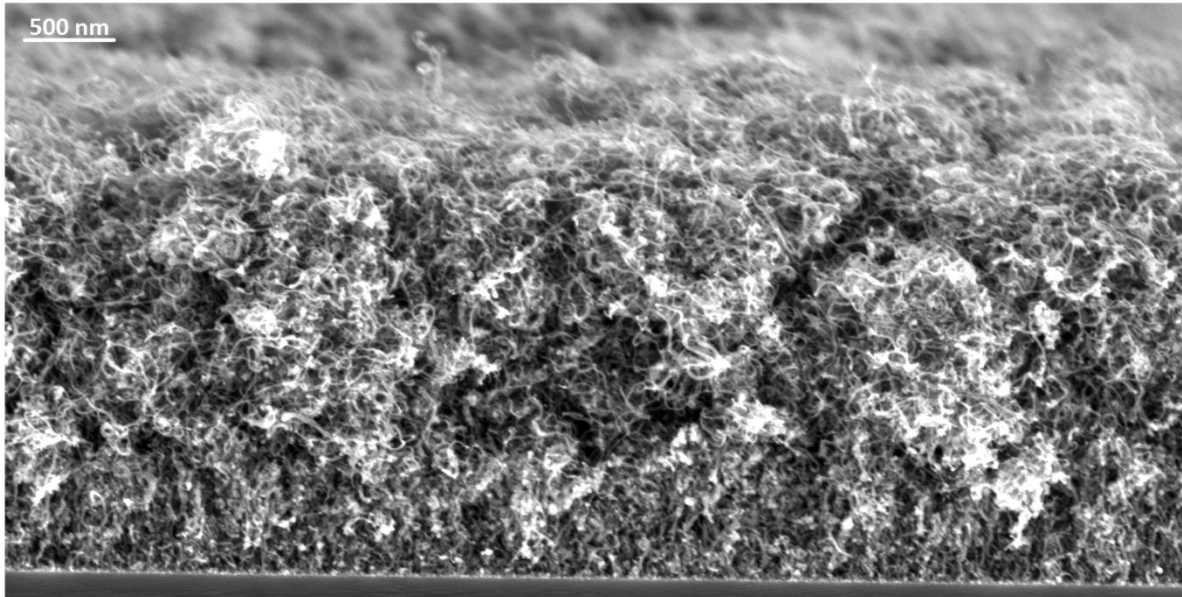
The radiative properties of the VO₂-CNT composite film, *i.e.*, emissivity (E) and reflectance (R), were computed using the Transfer Matrix Method for incoherent light³⁶. The assumption of incoherent light transport in the CNT film is justified, because of multiple scattering of light as a result of the large porosity of film. The model considers a 3 μm thick film over a semi-infinite silica substrate. Thus, the emissivity is computed as $E = 1 - R$. All the results are based on unpolarized light, *i.e.*, $R = 1/2(R^{(s)} + R^{(p)})$, where s and p , represent the two polarizations.

The optical properties of graphite³⁷ and silicon³⁸, are reported elsewhere. The dielectric constant of VO₂, together with the temperature-dependent model for hysteresis, were extracted from Wan et al.³⁹. In all the calculations, $\rho = 0.2$ and $R_{\text{CNT}} = 5$ nm, estimated from previously reported CVD grown CNTs films²⁹. The lattice constant was estimated as, $a = 20R_{\text{CNT}}$ ($\sim 0.8\%$ filling fraction), by fitting the spectral-averaged reflectance using the optical properties of the CNT film (Eqs. 2a and 2b, with $f_{\text{VO}_2} = 0$), with the reflectance from measurements for as-grown CNT ($\sim 2.5\%$).

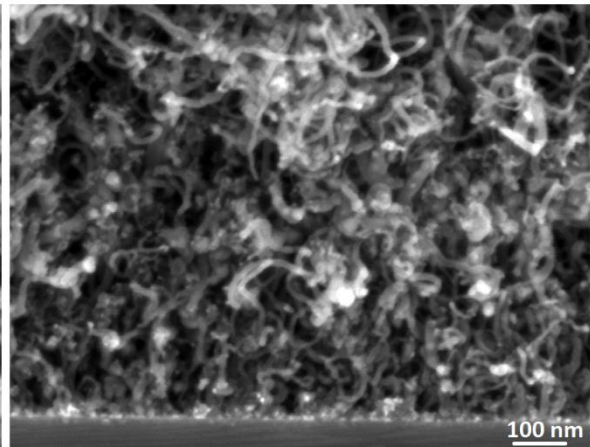
Results and discussion

Vanadium oxide layer is grown directly without any prior treatment of the CNTs. The present defect sites on the surface of CNTs^{29,28}, act likely as the growth centres for the ALD of oxides⁴⁰. Figure 1 displays the morphology of the cut cross-section of pristine and ALD coated CNTs with a high magnification view at the surface and interface regions. The average diameter of the CNT, ~10 nm prior the ALD of VO_x, increases to ~25 nm across the thickness of the CNT film as shown in figure 1. The CNTs retain their randomly oriented morphology, tubular structure and smooth surface. Furthermore, the apparent diameter is similar at the surface and deep at the interface with the substrate. These observations confirm the conformal nature of the vanadium oxide ALD deposition and the total infiltration across the porous CNT coating. The VO_x/CNTs radius was then monitored as a function of the number of VO_x-ALD cycles. A linear increase with the number of ALD cycles is observed with neither surface promotion nor inhibition of the growth as displayed in the figure S1. A deposition rate of 0.017 nm/cycle is measured on CNT while a higher growth rate of 0.03 nm/cycles is observed on planar silicon substrate. The relatively slow growth on the CNT might be attributed to the reduced density of nucleation sites on CNT.

Pristine CNTs Overview



near the surface



near the silicon interface

As-grown VO_x-CNT Overview

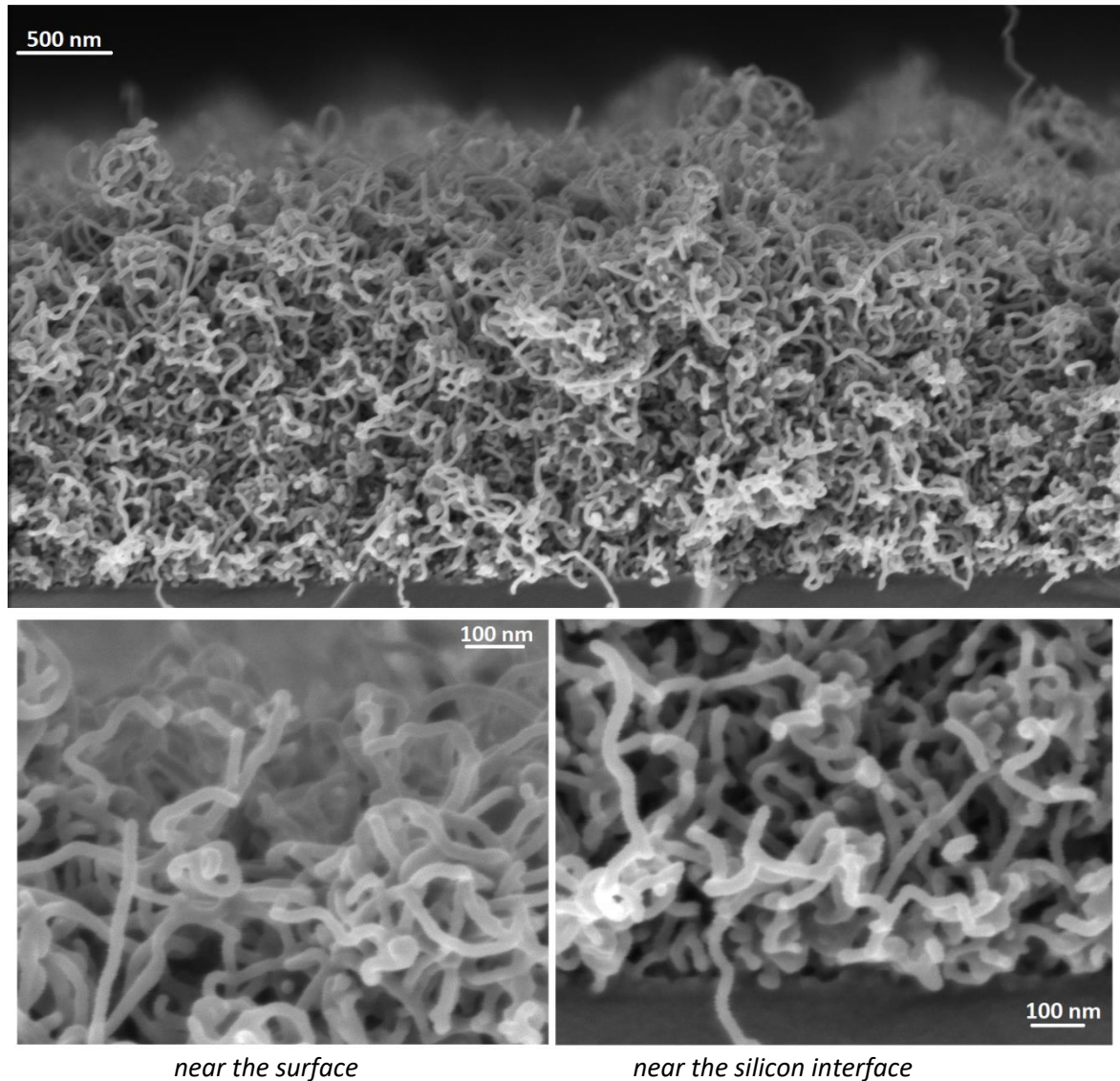


Figure 1: SEM Cross-section inspection of pristine CNTs with thickness of 3 μm , ($\phi_{\text{CNT}}=10\text{ nm}$) with high magnification view in the near surface and interface regions (top). Similar observation is displayed for ALD coated CNTs with 327 cycles of VO_x showing an apparent CNT diameter increase to reach $\sim 25\text{ nm}$ both near the surface and the silicon interface (bottom).

The as-grown films on CNTs are identified as amorphous or poorly crystalline V₂O₅ (Figure S2). Once the CNTs/V₂O₅ core/shell structure is obtained, a post deposition treatment is necessary to secure the conversion to CNTs/VO₂. For this purpose, heat treatment in vacuum (10^{-2} mbar) at 500 °C was performed. The density of the as-grown vanadium oxide is likely to be similar to that of V₂O₅, 3.36 g/cm³, or slightly lower. Whereas after conversion to crystalline VO₂, the film density would increase to 4.57 g/cm³. This change in the density was quantified in an earlier study devoted to the ALD of VO_x on planar silicon substrates³⁰. As a consequence, annealing might cause a significant surface morphology change such as roughening and de-wetting^{41,42}. In line with these expectations, significant surface roughening was observed as a result of post-deposition annealing as displayed in figure 2. Annealing thin VO_x (327 cycles) film results in a discontinuous VO₂ layer decorating the CNTs, whereas

thick layer of VO_x (1635 cycles) on CNTs yields continuous VO_2 layer on CNTs with perceptible surface roughening.

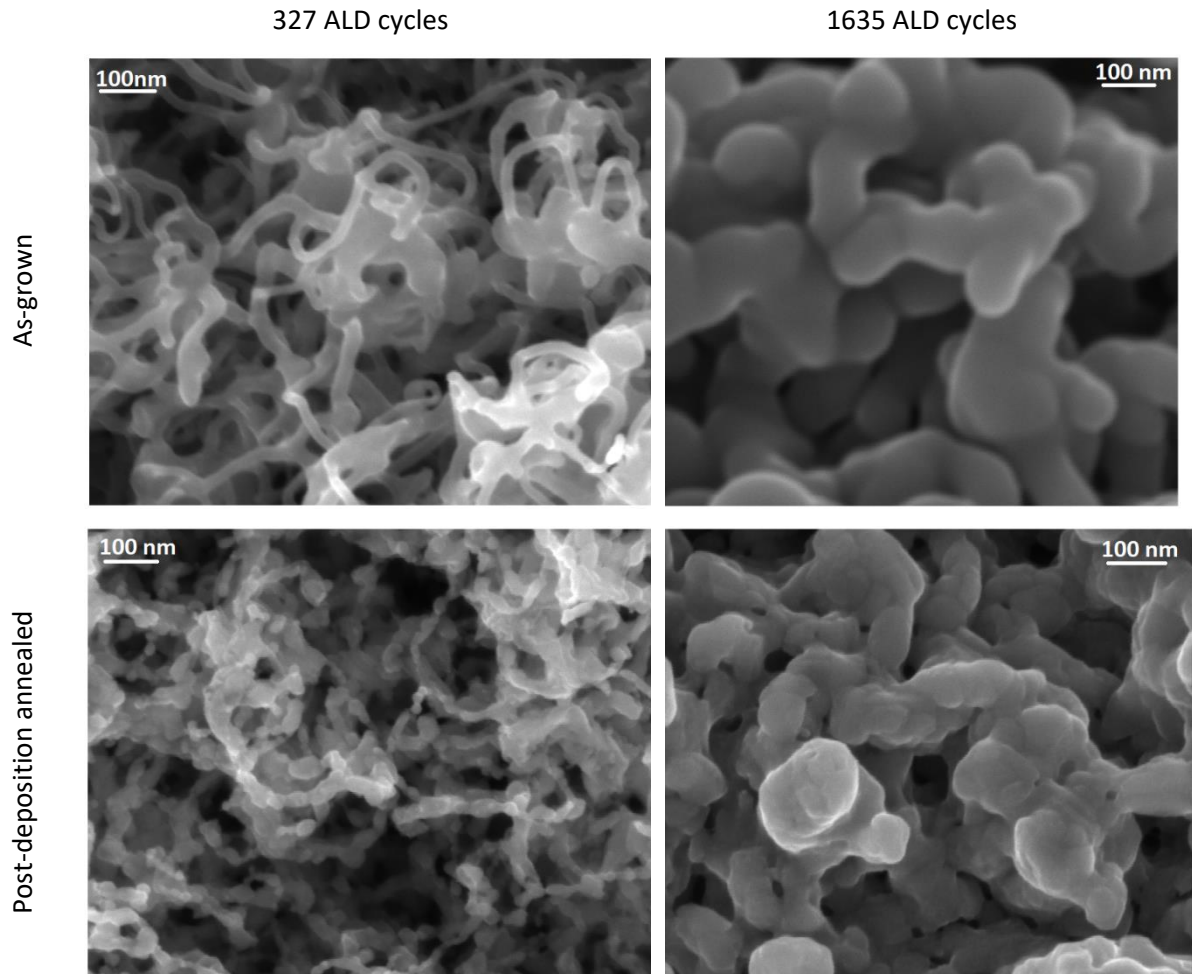


Figure 2. SEM surface inspection of the ALD grown VO_x on CNT: 327 cycles (VO_2 decorated) (left), 1635 cycles (VO_2 covered) (right), before (top) and after (bottom) conversion to VO_2 .

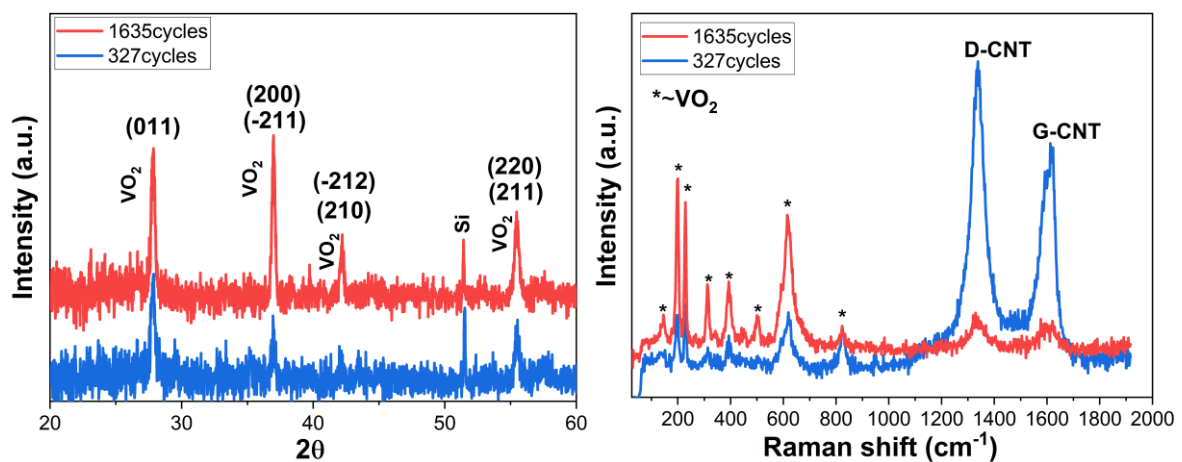


Figure 3. XRD (left) and Raman scattering (right) on VO_2 decorated (327 cycles) and covered (1635 cycles) CNTs.

Raman analysis provides evidence that post deposition annealing in vacuum has converted films into VO_2 phase. The appearance of Raman V-V low frequency vibrational modes at 146, 196 and 227 cm^{-1}

in addition to the V-O high frequency vibrational modes 313, 394 and 617 cm^{-1} are in line with the presence of VO_2 phase³⁰, as shown in the figure 3. The detection of CNTs “D” vibration modes at 1337 cm^{-1} and “G” vibration modes at 1612 cm^{-1} confirms the preservation of CNTs after annealing at high temperatures, in the CNTs/ VO_2 - core/shell structure. Here the “G” mode corresponds to the in-plane oscillation of the crystalline graphite and “D” mode corresponds oscillation of the defective amorphous carbon²⁹. The bands attributed to VO_2 intensify with the number of ALD cycles at the expense of the CNT bands.

XRD analysis of annealed films, as shown in figure 3, confirms the formation of polycrystalline VO_2 monoclinic phase (pdf n° 04-003-2035 [28]). Single peak analysis as described in the experimental part was implemented to extract the crystallite size by fitting the (011) peak at 27.83° to the pseudo voigt1 function⁴³. The calculated crystallite size for the discontinuous nanostructure VO_2 (327 cycles) is approximately 55 nm, whereas a plateau at ~120 nm is observed for continuous VO_2 layers on CNTs as shown in figure S3. This result reasonably fits to the observed morphology by SEM.

The grain boundary area (γ) depends on both the crystallite size and the film thickness, featuring an exponential decay when crystallites are assumed to exhibit a spherical shape⁴⁴. Here the calculated γ was normalized to the volume of VO_2 layer to obtain the $\text{GB} = \gamma/\text{volume}$. In figure S3, we can see that the GB decreases gradually with increased number of VO_x ALD cycles. While the crystallite size features a saturation behaviour.

VO_2 -decorated CNTs (327 cycles) feature a low strain relative to VO_2 covered CNTs (>625 cycles) as shown in figure S3. Referring to the evaluated uncertainty on the determination of the strain, the observed difference as a function of the number of ALD cycles can be considered marginal for all VO_2 -covered CNTs (>625 ALD cycles of vanadium oxide). Here we assume that strain in ultrathin VO_2 (327 cycle) film is relaxed by the formation of disconnected nanoparticles on the CNT surface. The calculated strain values for VO_2 -covered CNTs are in a similar range as the one measured for the strained VO_2 nanobeams on SiO_2 substrate⁴⁵. The type of strain can hardly be obtained from the XRD measurement where the peak shift 2θ value is very small relative to unstrained single crystal VO_2 . The Raman peak in VO_2 -CNTs nanocomposite shifts however towards higher frequencies (cm^{-1}) relative to the single crystal VO_2 ⁴⁶, which is attributed to the presence of compressive strain in the film. The “c” lattice parameter features an abrupt change from 5.755 Å in the semiconducting, to 5.700 Å in the metallic VO_2 across the transition, which is due to the orbital occupancy at the fermi level. As the SMT comes with a shrinkage of the lattice, it is favoured at lower temperatures when the semiconducting phase features a compressive strain⁴⁷. As is reported earlier, the SMT temperature increases above

67 °C for the tensile strained films and decreases below 67 °C for the compressive strain in VO₂ films^{48,45}, which is in line with the observed behaviour in the figure S3.

The temperature-dependent optical properties of the nanocomposite VO₂/CNTs shell/core coating were investigated using a thermal camera and a UV-VIS NIR spectrometer. As these composite films are opaque and porous in nature, total hemispherical reflection (THR) is well suited to investigate their diffuse optical properties. The SMT behaviour of VO₂/CNTs was monitored in the spectral range from 300 to 2300 nm. The resulting temperature-dependent measurements are displayed in figure 4 for VO₂-decorated and VO₂-covered CNTs.

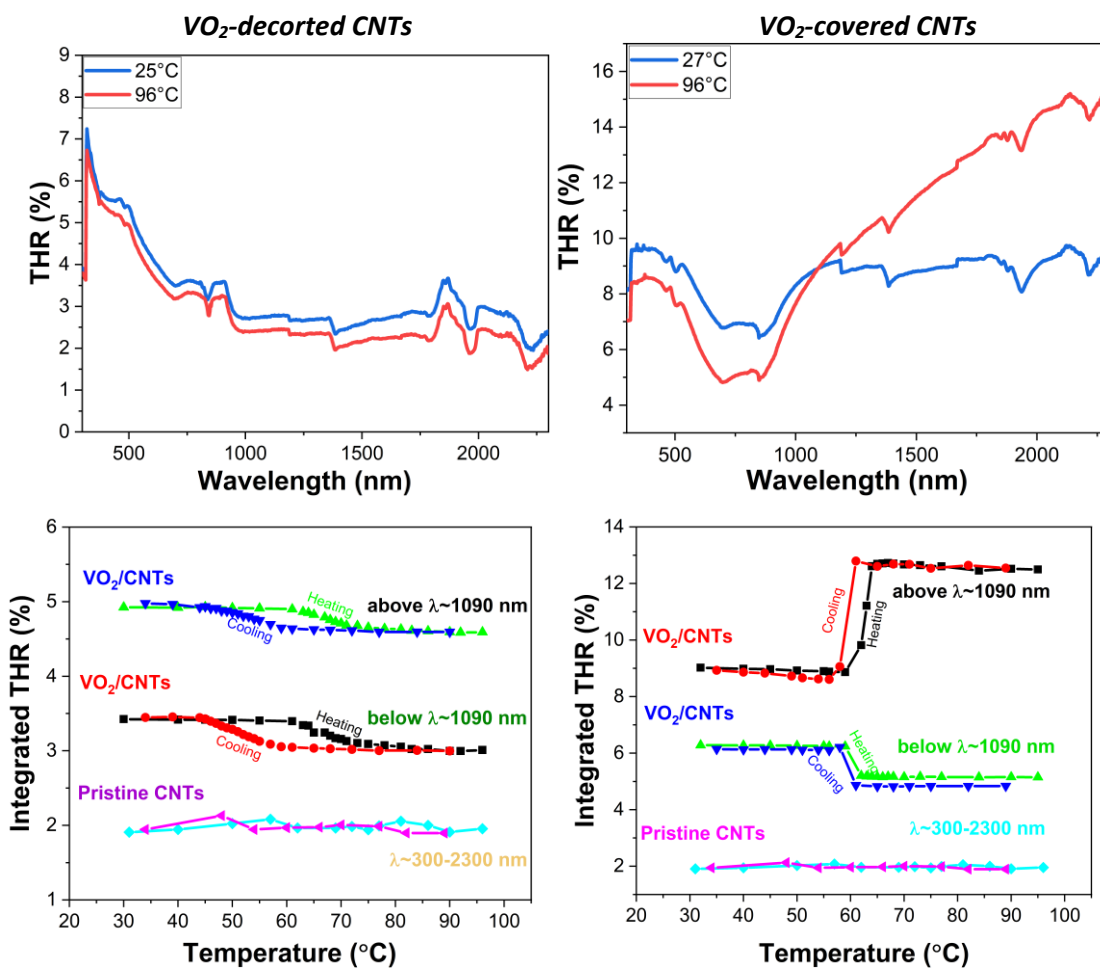


Figure 4. Temperature-dependent Total Hemispherical Reflectance (THR) upon heating as a function of the wavelength and the variation of the integrated THR at the inflecting point across the transition temperature upon consecutive heating and cooling of VO₂-decorated CNTs (left), VO₂-covered CNTs (right).

VO₂-covered CNTs show an increase in the reflectance for $\lambda > 1100$ nm in the near infrared and a decrease for $\lambda < 1100$ nm in the UV-VIS-NIR region across the SMT, while the VO₂-decorated CNTs show a decrease of the total hemispherical reflectance in the entire investigated spectral range.

The reflectance curves obtained from modelling (Figure 5), show a qualitatively good agreement with the experiments (Figure 4). A major discrepancy between the results from simulation and experiments is observed in the decorated CNTs case; the former shows a monotonic growth with the wavelength, as opposed to the later. The discrepancy is a consequence of the effective media model considered (Eqs.2a and 2b), which neglects near-field interactions between the CNTs. In the case of covered CNTs the discrepancy becomes less evident, as the optical response becomes more dominated by the optical properties from VO₂, which are more accurately represented by the Bruggemann's model (Eq. 5).

The simulations allow to explain the experimental observations and its relation to the filling fraction of VO₂. Indeed, the filling fraction of VO₂ in the VO₂-decorated CNTs is below the percolation threshold, and the coating is mainly distributed in small domains³⁵. The larger absorption in the hot (metallic) phase is, thus, a consequence of localized surface plasmons excitation, induced by the interaction of light and the confined VO₂ domains. In the case of VO₂-covered CNTs the filling fraction of VO₂ is above the percolation threshold, forming large domains that behave as a continuum³⁵. Thus, the coating becomes more reflective in the hot (metallic) phase as compared to the cold phase.

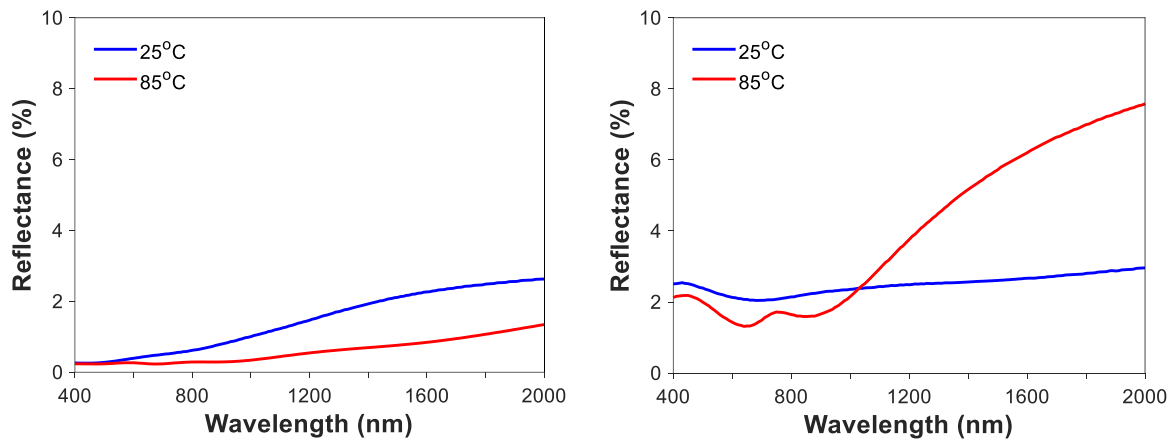


Figure 5. Simulated reflectance at normal incidence for (left) VO₂-decorated (625 cycles) and (right) VO₂-covered (1365 cycles).

Next, thermal emissivity as a function of temperature of VO₂-decorated and VO₂-covered CNTs films is investigated (Figure 6). The results consider the spectral and hemispherical averaged emissivity in the mid infrared region i.e. λ : 3 – 5 μm . The SMT transition in VO₂ in both cases, induces a modulation of the emissivity ($\Delta E = E^{hot} - E^{cold}$). The modulation is either, upward ($\Delta E > 0$), for decorated (low number of ALD-cycles), or downward ($\Delta E < 0$) for covered (high number of ALD-cycles) CNTs. These results are consistent with the aforementioned observations for the reflectance measurements in the 0.4-2 μm spectral range. Similar emissivity modulation results are obtained for decorated/covered VO₂ films on silicon substrate (Figure S4).

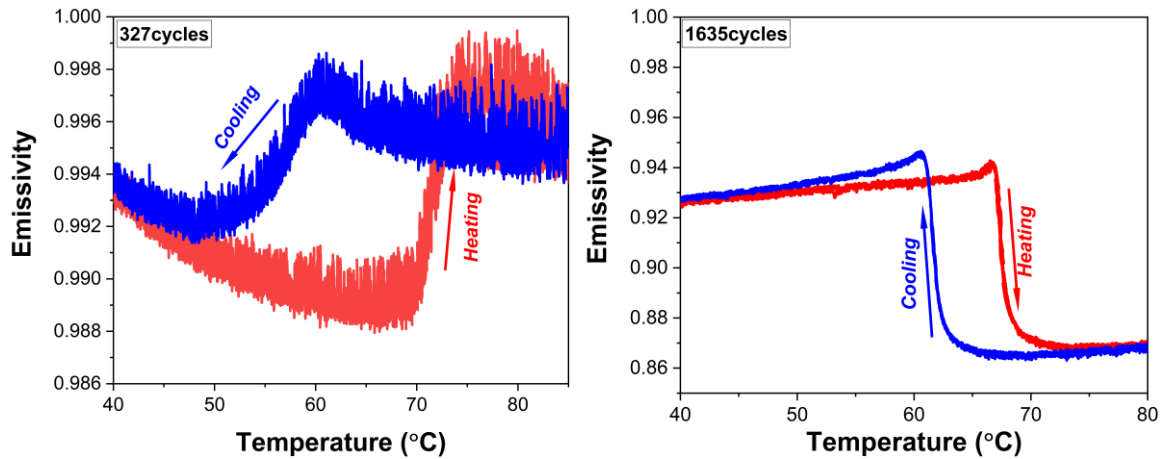


Figure 6. Emissivity measurements of the VO_2 -decorated CNTs (left), VO_2 -covered CNTs (right) nanocomposite films.

Additionally, both emissivity curves show a peak near the transition region. The results for calculated spectral and hemispherical average emissivity are consistent with the results from measurements (Figure 7), and able to capture the most relevant features of the phenomenon, *i.e.*, degree and sign of emissivity modulation, and maximum peak near the transition. The difference in the transition temperatures, as well as the hysteresis width (ΔH) are due to hysteresis model considered³⁹. Similar to the aforementioned observation from the reflectance plots (Figure 5), the switching in the emissivity modulation ($\Delta E > 0$ for decorated samples and $\Delta E < 0$ for covered samples), is a consequence of the filling fraction of VO_2 in relation with the percolation threshold. Interestingly the peak in the emissivity near the transition region is clearly displayed from the model. This peak corresponds to localized surface plasmon resonances induced by the small metallic domains present at the metastable phase across the semiconductor-to-metallic transition, in line with previously reported measurements^{9,49,50}.

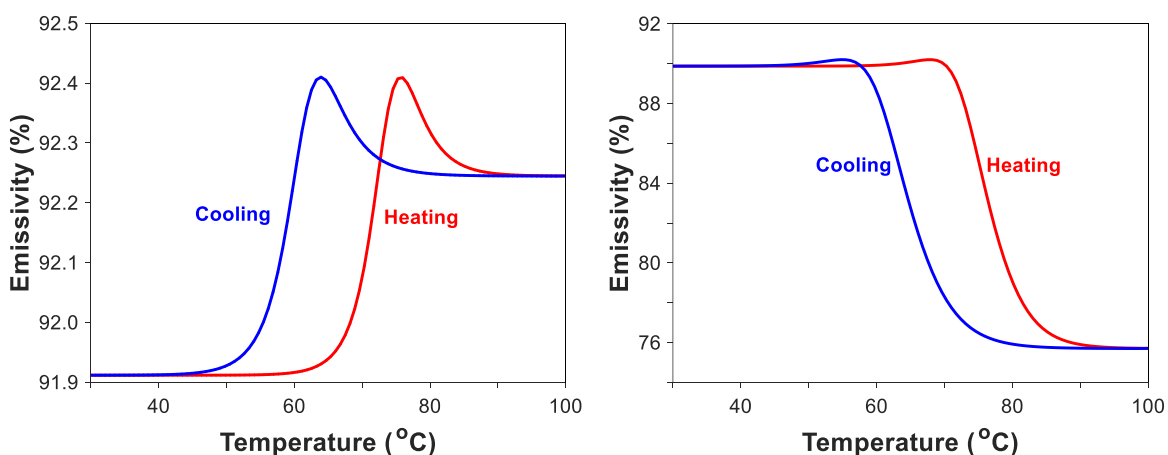


Figure 7 Simulated spectral and hemispherical averaged emissivity as a function of temperature for (left) VO_2 -decorated (327 cycles), and (right) VO_2 -coated (1635 cycles). Results consider a complete heating and cooling cycle.

The percolation threshold marks a turning point for modulation of the optical properties in VO_2 -CNTs composites. It is therefore customary to predict the threshold based on the theoretical model.

However, given the complexity of Eq. (2), the solution cannot be determined analytically, and thus the value is estimated from graphical results. The percolation threshold is estimated as, 11.35% filling fraction that correspond to 862 ALD cycles, based on the crossing of the hot and cold state curves of the spectral and hemispherical average reflectance as a function of the number of ALD cycles (Figure 8). From figure 9, it can be noticed that experimentally the percolation threshold value corresponds to 625 ALD cycles, based on the crossing of hot and cold state hemispherical emissivity (3-5 μm). For lower ALD cycles, average hemispherical reflectance (emissivity) decreases (increases), while in case of higher ALD cycles average hemispherical reflectance (emissivity) increases (decreases).

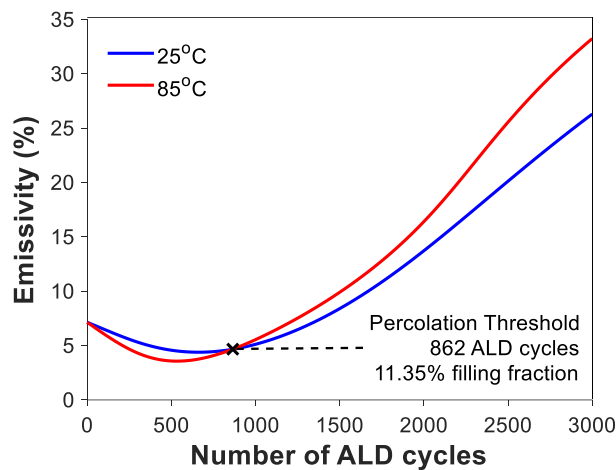


Figure 8. Estimation of percolation threshold. Average spectral and hemispherical reflectance for hot a cold state of VO_2 –CNTs films as function of the number of ALD cycles.

Temperature-triggered emissivity modulation features a hysteresis, the derivative of which (dE/dT) is used to extract characteristic parameters. The sharpness of the SMT is discussed referring to the parameter $1/\Delta T$. Earlier report correlates sharp transitions (high $1/\Delta T$ values) and narrow hysteresis to a large grain sizes (r) and low grain boundary area (γ)⁵¹. The estimated GB decreases with the increased number of ALD cycles of VO_x on the CNTs (**Error! Reference source not found.S3**). Low GB is therefore associated with low defect concentration, as defects are more likely to occur at the interface between grains forming the film. In line with this reasoning, we observed narrow hysteresis (ΔH) and sharper transitions ($1/\Delta T$) with decreased GB, as shown in the figure 9.

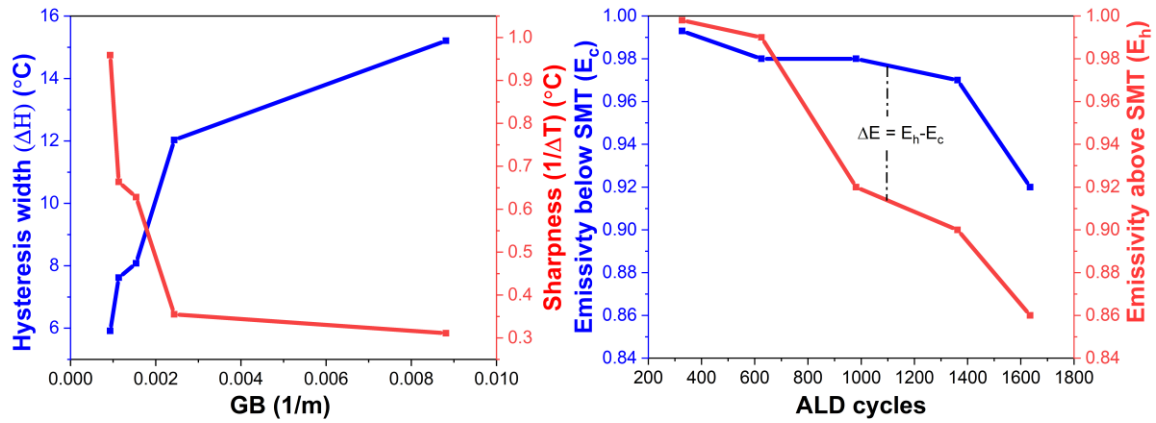


Figure 9. Hysteresis width (ΔH) and transition sharpness ($1/\Delta T$) variation with the ALD cycles (left); Emissivity modulation amplitude across SMT for varied ALD cycles composite film (right).

Here we addressed the challenge of establishing a design approach to trigger an upward and downward emissivity modulation while using the same building blocks. Simulation efforts were also implemented to link this behaviour to the percolation threshold and the physics of metallic nanoparticles versus bulk films. Further developments towards efficient implementation would require the optimization of the modulation amplitude. In this respect, introducing an intermediate dielectric layer^{15,16} is expected to play a significant role. If VO₂/CNTs nanocomposite film is implemented as a smart solar absorber, the abrupt upward emissivity modulation across the SMT would slow-down the surface heating as a response to heating above the transition. An increased heat capture is however expected for nanocomposites featuring a downward emissivity modulation. The last would therefore feature an enhanced solar selective absorption above the SMT.

Conclusion

VO₂-CNTs nanocomposite films are developed using a hybrid CVD/ALD process with the objective to tailor the light absorption behaviour. The modulation of the optical properties induced by the phase-change on VO₂ inclusions appeared to be strongly dependent on the filling fraction. Thus, at small numbers of ALD cycles the emissivity(reflectivity) of the film was switched upward(downward) across the SMT, while the opposite was observed at large numbers of ALD cycles. The results were successfully explained by effective media theory, and a theoretical model to predict the optical response of the VO₂-CNT composite film was derived. The model allowed to determine the percolation threshold over which the VO₂ inclusions start forming a continuum domain with bulk-like behaviour. Below this threshold, the VO₂ inclusions are confined in small domains that feature a larger absorption in the IR region at the metallic phase, due to the excitation of localized surface plasmons. Above the threshold the VO₂ inclusions form a large continuum that becomes more reflective in the

metallic phase. The developed nanocomposite coatings can be implemented in different applications as a smart absorber or smart radiator, temperature sensors, and photothermal actuators

Acknowledgements

Vasu Prasad Prasadam and Naoufal Bahlawane would like to acknowledge funding through the MASSENA Pride program of the Luxembourg National Research Fund (project ID: FNR PRIDE/MASSENA/15/10935404). Francisco V. Ramirez and Ioannis Papakonstantinou would like to thank the European Research Council for a starting grant ERC-StG-IntelGlazing, project ID: 679891. Ivan P. Parkin thanks the EPSRC for the grant EP/L015862/1

References

1. IEA. Global Energy & CO₂ Status Report: Emissions. *iea.org*. 2019:15. <https://webstore.iea.org/global-energy-co2-status-report-2017>. Accessed May 23, 2019.
2. Granqvist, C.G. Spectrally selective coatings for energy efficiency and solar applications. *Phys Scr*. 1985;32(4):401-407. doi:10.1088/0031-8949/32/4/026
3. Wang, L.P.; Lee, B.J.; Wang, X.J.; Zhang, Z.M. Spatial and temporal coherence of thermal radiation in asymmetric Fabry-Perot resonance cavities. *Int J Heat Mass Transf*. 2009;52(13-14):3024-3031. doi:10.1016/j.ijheatmasstransfer.2009.01.042
4. Granqvist, C.G. ENERGY-EFFICIENT WINDOWS: PRESENT AND FORTHCOMING TECHNOLOGY. In: *Materials Science for Solar Energy Conversion Systems*. Pergamon; 1991:106-167. doi:10.1016/b978-0-08-040937-5.50009-7
5. Bahlawane, N.; Pachot, C.; Lafont, U. Innovative CNT-based composite coatings for the stray light reduction. *Proc SPIE - Int Soc Opt Eng*. 2017;10562(October):1-9. doi:10.1117/12.2296152
6. Bahlawane, N.; Lenoble, D. Vanadium Oxide Compounds : Structure , Properties , and Growth from the Gas Phase. 2014:299-311. doi:10.1002/cvde.201400057
7. Prasadam, V.P; Bahlawane, N.; Mattelaer, F.; Rampelberg, G.; Detavernier, C.; Fang, L.; Jiang, Y.; Martens, K.; Parkin, I. P.; Papakonstantinou, I. Atomic layer deposition of vanadium oxides: process and application review. *Mater Today Chem*. 2019;12:396-423.

- doi:10.1016/j.mtchem.2019.03.004
8. Voti, R.L.; Larciprete, M.C.; Leahu, G.; Sibilia, C.; Bertolotti, M. Optimization of thermochromic VO₂ based structures with tunable thermal emissivity. *J Appl Phys.* 2012;112(3). doi:10.1063/1.4739489
 9. Kumar, S.; Maury, F.; Bahlawane, N. Light modulation in phase change disordered metamaterial - A smart cermet concept. *Mater Today Phys.* 2017;3(December):41-47. doi:10.1016/j.mtphys.2017.12.002
 10. Wang, S.; Liu, G.; Hu, P.; Zhou, Y.; Ke, Y.; Li, C.; Chen, J.; Cao, T.; Long, Yi. Largely Lowered Transition Temperature of a VO₂/Carbon Hybrid Phase Change Material with High Thermal Emissivity Switching Ability and Near Infrared Regulations. *Adv Mater Interfaces.* 2018;5(21):1-8. doi:10.1002/admi.201801063
 11. Xiao, L.; Ma, H.; Liu, J.; Zhao, W.; Jia, Y.; Zhao, Q.; Liu, K.; Wu, Y.; Wei, Y.; Fan, S.; Jiang, K. Fast Adaptive Thermal Camouflage Based on Flexible VO₂/Graphene/CNT Thin Films. *Nano Lett.* 2015;15(12):8365-8370. doi:10.1021/acs.nanolett.5b04090
 12. Yang, L.; Zhou, P.; Huang, T.; Zhen, G.; Zhang, L.; Bi, L.; Weng, X.; Xie, J.; Deng, L. Broadband thermal tunable infrared absorber based on the coupling between standing wave and magnetic resonance. *Opt Mater Express.* 2017;7(8):2767. doi:10.1364/ome.7.002767
 13. Gomez-Heredia, C.L.; Ramirez-Rincon, J.A.; Ordonez-Miranda, J.; Ares, O.; Alvarado-Gil, J. J.; Champeaux, C.; Dumas-Bouchiat, F.; Ezzahri, Y.; Joulain, K. Thermal hysteresis measurement of the VO₂ emissivity and its application in thermal rectification. *Sci Rep.* 2018;8(1):1-11. doi:10.1038/s41598-018-26687-9
 14. Benkahoul, M.; Chaker, M.; Margot, J.; Haddad, E.; Kruzelecky, R.; Wong, B.; Jamroz, W.; Poinas, P. Thermochromic VO₂ film deposited on Al with tunable thermal emissivity for space applications. *Sol Energy Mater Sol Cells.* 2011;95(12):3504-3508. doi:10.1016/j.solmat.2011.08.014
 15. Hendaoui, A.; Émond, N.; Dorval, S.; Chaker, M.; Haddad, E. VO₂-based smart coatings with

- improved emittance-switching properties for an energy-efficient near room-temperature thermal control of spacecrafts. *Sol Energy Mater Sol Cells*. 2013;117:494-498. doi:10.1016/j.solmat.2013.07.023
16. Sun, K.; Riedel, C.A.; Urbani, A.; Simeoni, M.; Mengali, S.; Zalkovskij, M.; Bilenberg, B.; De Groot, C. H.; Muskens, O.L. VO₂ Thermo-chromic Metamaterial-Based Smart Optical Solar Reflector. *ACS Photonics*. 2018;5(6):2280-2286. doi:10.1021/acsphotonics.8b00119
 17. Taylor, A.; Parkin, I.; Noor, N.; Tummeltshammer, C.; Brown, M.S.; Papakonstantinou, I. A bioinspired solution for spectrally selective thermo-chromic VO₂ coated intelligent glazing. *Opt Express*. 2013;21(S5):A750. doi:10.1364/OE.21.00A750
 18. Wu, S.H.; Chen, M.; Barako, M.T.; Jankovic, V.; Hon, P.W. C.; Sweatlock, L. A.; Povinelli, M. Thermal homeostasis using microstructured phase-change materials. *Optica*. 2017;4(11):1390. doi:10.1364/OPTICA.4.001390
 19. Powell, M.J.; Quesada-Cabrera, R.; Taylor, A.; Teixeira, D.; Papakonstantinou, I.; Palgrave, R.; Sankar, G.; Parkin, I.P. Intelligent Multifunctional VO₂/SiO₂/TiO₂ Coatings for Self-Cleaning, Energy-Saving Window Panels. *Chem Mater*. 2016;28(5):1369-1376. doi:10.1021/acs.chemmater.5b04419
 20. Haddad, E.; Kruzelecky, R. V.; Wong, B.; Jamroz, W.; Soltani, M.; Benkahoul, M.; Chaker, M.; Poinas, P. Multilayer Tuneable Emittance Coatings with Low Solar Absorptance for Improved Smart Thermal Control in Space Applications. *SAE Tech Pap Ser*. 2010;1. doi:10.4271/2009-01-2575
 21. Chao, D.; Zhu, C; Xia, X, et al. Graphene quantum dots coated VO₂ arrays for highly durable electrodes for Li and Na ion batteries. *Nano Lett*. 2015;15(1):565-573. doi:10.1021/nl504038s
 22. Evans, G.P.; Powell, M.J.; Johnson, I.D.; Howard, D.; Bauer, D.; Darr, J.A.; Parkin, I.P. Room temperature vanadium dioxide-carbon nanotube gas sensors made via continuous hydrothermal flow synthesis. *Sensors Actuators, B Chem*. 2018;255:1119-1129. doi:10.1016/j.snb.2017.07.152

23. Ma, H.; Zhang, X.; Zhang, Z.; Wang, Y.; Wang, G.; Liu, F.; Cui, R.; Huang, C.; Wang, M.; Wei, Y.; Jiang, K.; Pan, L.; Liu, K. Infrared micro-detectors with high sensitivity and high response speed using VO₂-coated helical carbon nanocoils. *J Mater Chem C*. 2019;7(39):12095-12103. doi:10.1039/c9tc02833a
24. Ma, H.; Hou, J.; Wang, X.; Zhang, J.; Yuan, Z.; Xiao, L.; Wei, Y.; Fan, S.; Jiang, K.; Liu, K. Flexible, all-inorganic actuators based on vanadium dioxide and carbon nanotube bimorphs. *Nano Lett*. 2017;17(1):421-428. doi:10.1021/acs.nanolett.6b04393
25. Wang, Y.; Zhang, L.; Wang, P. Self-Floating Carbon Nanotube Membrane on Macroporous Silica Substrate for Highly Efficient Solar-Driven Interfacial Water Evaporation. *ACS Sustain Chem Eng*. 2016;4(3):1223-1230. doi:10.1021/acssuschemeng.5b01274
26. Wang, T.; Torres, D.; Fernández, F.E.; Wang, C.; Sepúlveda, N. Maximizing the performance of photothermal actuators by combining smart materials with supplementary advantages. *Sci Adv*. 2017;3(4):1-10. doi:10.1126/sciadv.1602697
27. Ma, H.; Zhang, X.; Cui, R.; Liu, F.; Wang, M.; Huang, C.; Hou, J.; Wang, G.; Wei, Y.; Jiang, K.; Pan, L.; Liu, K. Photo-driven nanoactuators based on carbon nanocoils and vanadium dioxide bimorphs. *Nanoscale*. 2018;10(23):11158-11164. doi:10.1039/c8nr03622e
28. Basheer, H.J.; Baba, K.; Bahlawane, N. Thermal Conversion of Ethanol into Carbon Nanotube Coatings with Adjusted Packing Density. *ACS Omega*. 2019;4(6):10405-10410. doi:10.1021/acsomega.9b00616
29. Basheer, H.J.; Pachot, C.; Lafont, U.; Devaux, X.; Bahlawane, N. Low-Temperature Thermal CVD of Superblack Carbon Nanotube Coatings. *Adv Mater Interfaces*. 2017;4(18):1-9. doi:10.1002/admi.201700238
30. Prasad, V.P.; Dey, B.; Bulou, S.; Schenk, T.; Bahlawane, N. Study of VO₂ thin film synthesis by atomic layer deposition. *Mater Today Chem*. 2019;12:332-342. doi:10.1016/j.mtchem.2019.03.005
31. García-Vidal, F.J.; Pitarke, J.M.; Pendry, J.B. Effective medium theory of the optical properties

- of aligned Carbon nanotubes. *Phys Rev Lett.* 1997;78(22):4289-4292.
doi:10.1103/PhysRevLett.78.4289
32. Henrard, L.; Lambin, P. Calculation of the energy loss for an electron passing near giant fullerenes. *J Phys B At Mol Opt Phys.* 1996;29(21):5127-5141. doi:10.1088/0953-4075/29/21/024
33. García-Vidal, F.J.; Pitarke, J.M. Optical absorption and energy-loss spectra of aligned carbon nanotubes. *Eur Phys J B.* 2001;22(2):257-265. doi:10.1007/PL00011146
34. Banhegyi, G. Comparison of electrical mixture rules for composites. *Colloid Polym Sci.* 1986;264(12):1030-1050. doi:10.1007/BF01410321
35. Cai, W.; Shalaev, V. *Optical Metamaterials: Fundamentals and Applications.* Springer; 2009.
36. Katsidis, C.C.; Siapakas, D.I. General transfer-matrix method for optical multilayer systems with coherent, partially coherent, and incoherent interference. *Appl Opt.* 2002;41(19):3978. doi:10.1364/AO.41.003978
37. Djurišić, A.B.; Li, E.H. Optical properties of graphite. *J Appl Phys.* 1999;85(10):7404-7410. doi:10.1063/1.369370
38. Palik, E.D.; Ghosh, G. *Handbook of Optical Constants of Solids.* 1st ed. Academic Press; 1998.
39. Wan, C.; Zhang, Z.; Woolf, D.; Hessel, C.; Rensberg, J.; Hensley, J.M.; Xiao, Y.; Shahsafi, A.; Salman, J.; Richter, S.; Sun, Y.; Qazilbash, M.M.; Schmidt-Grund, R.; Ronning, C.; Ramanathan, S.; Kats, M.A. On the Optical properties of thin-film vanadium dioxide from the visible to the far infrared. *Ann Phys.* 2019;1900188:1-7. doi:10.1002/andp.201900188
40. Stano, K.L.; Carroll, M.; Padbury, R.; McCord, M.; Jur, J.S.; Bradford, P.D. Conformal atomic layer deposition of alumina on millimeter tall, vertically-aligned carbon nanotube arrays. *ACS Appl Mater Interfaces.* 2014;6(21):19135-19143. doi:10.1021/am505107s
41. Rampelberg, G.; Deduytsche, D.; De Schutter, B.; Premkumar, P.A.; Toeller, M.; Schaeckers, M.; Martens, K.; Radu, I.; Detavernier, C. Crystallization and semiconductor-metal switching behavior of thin VO₂ layers grown by atomic layer deposition. *Thin Solid Films.* 2014;550:59-

64. doi:10.1016/j.tsf.2013.10.039
42. Peter, A.P.; Martens, K.; Rampelberg, G.; Toeller, M.; Ablett, J.; Meersschaut, J.; Cuypers, D.; Franquet, A.; Detavernier, C.; Rueff, J.P.; Schaekers, M.; Van Elshocht, S.; Jurczak, M.; Adelman, C.; Radu, I.P. Metal-insulator transition in ALD VO₂ ultrathin films and nanoparticles: Morphological control. *Adv Funct Mater.* 2015;25(5):679-686. doi:10.1002/adfm.201402687
43. De Keijser, T.H.; Langford, J.I.; Mittemeijer, E.J.; Vogels, A.B.P. *Use of the Voigt Function in a Single-Line Method for the Analysis of X-Ray Diffraction Line Broadening.* Vol 15.; 1982.
44. Siegel, R.W.; Thomas, G.J. Grain boundaries in nanophase materials. *Ultramicroscopy.* 1992;40(3):376-384. doi:10.1016/0304-3991(92)90135-7
45. Park, J.H.; Coy, J.M.; Serkan, K.T.; Huang, C.; Fei, Z.; Hunter, S.; Cobden, D.H. Measurement of a solid-state triple point at the metal-insulator transition in VO₂. *Nature.* 2013;500(7463):431-434. doi:10.1038/nature12425
46. Parker, J.C. Raman scattering from VO₂ single crystals: A study of the effects of surface oxidation. *Phys Rev B.* 1990;42(5):3164-3166. doi:10.1103/PhysRevB.42.3164
47. Aetukuri, N.B.; Gray, A.X.; Drouard, M.; Cossale, M.; Gao, L.; Reid, A.H.; Kukreja, R.; Ohldag, H.; Jenkins, C.A.; Arenholz, E.; Roche, K.P.; Dürr, H.A.; Samant, M.; Parkin, S.S.P. Control of the metal-insulator transition in vanadium dioxide by modifying orbital occupancy. *Nat Phys.* 2013;9(10):661-666. doi:10.1038/nphys2733
48. Atkin, J.M.; Berweiger, S.; Chavez, E.K.; Raschke, M.B.; Cao, J.; Fan, W.; Wu, J. Strain and temperature dependence of the insulating phases of VO₂ near the metal-insulator transition. *Phys Rev B - Condens Matter Mater Phys.* 2012;85(2):1-4. doi:10.1103/PhysRevB.85.020101
49. Kats, M.A.; Sharma, D.; Lin, J.; Genevet, P.; Blanchard, R.; Yang, Z.; Qazilbash, M.M.; Basov, D. N.; Ramanathan, S.; Capasso, F. Ultra-thin perfect absorber employing a tunable phase change material. *Appl Phys Lett.* 2012;101(22). doi:10.1063/1.4767646
50. Kats, M.A.; Blanchard, R.; Zhang, S.; Genevet, P.; Ko, C.; Ramanathan, S.; Capasso, F. Vanadium dioxide as a natural disordered metamaterial: Perfect thermal emission and large broadband

negative differential thermal emittance. *Phys Rev X*. 2014;3(4):1-7.

doi:10.1103/PhysRevX.3.041004

51. Narayan, J.; Bhosle, V.M. Phase transition and critical issues in structure-property correlations of vanadium oxide. *J Appl Phys*. 2006;100(10). doi:10.1063/1.2384798

TOC

